Hydrol. Earth Syst. Sci. Discuss., 11, 411–449, 2014
www.hydrol-earth-syst-sci-discuss.net/11/411/2014/
doi:10.5194/hessd-11-411-2014

Hydrology and Earth System Sciences
Open Access
Discussions

Evaluation of TRMM 3B42 (TMPA) precipitation estimates and WRF retrospective precipitation simulation over the Pacific-Andean basin into Ecuador and Peru

A. Ochoa[1,3], **L. Pineda**[1,2], **P. Willems**[1], **and P. Crespo**[3]

[1]KU Leuven, Department of Civil Engineering, Hydraulics Laboratory, 3001 Leuven, Belgium
[2]Unidad de Ingeniería Civil, Geología y Minas, Universidad Técnica Particular de Loja, C/. Marcelino Champagnat S/N, Loja, Ecuador
[3]Grupo de Ciencias de la Tierra y del Ambiente, DIUC, Universidad de Cuenca, Av. Víctor Manuel Albornoz, Quinta Balzaín, Cuenca, Ecuador

Received: 17 December 2013 – Accepted: 31 December 2013 – Published: 10 January 2014

Correspondence to: L. Pineda (luis.pineda@bwk.kuleuven.be)

Published by Copernicus Publications on behalf of the European Geosciences Union.

Abstract

An important issue for the Pacific-Andean basin in western South-America is whether the latest satellite-based and Numerical Weather Prediction (NWP) model outputs, provide the potential to compensate data scarcity. Based on a comprehensive dataset of ground precipitation, the performance of the Tropical Rainfall Measuring Mission (TRMM) 3B42V7 and its predecessor version the 3B42V6, and the Weather Research Forecast (WRF) precipitation product (OA-NOSA30) are evaluated over 21 sub-catchments situated in the westernmost N-S axis of South America: the Pacific-Andean Basin in Ecuador and Peru (PAEP). In general, precipitation estimates from TRMM and OA-NOSA30 capture the seasonal features of precipitation in the study area. Quantitatively, only the Southern sub-catchments of Ecuador and Northern Peru (3.6–6° S) are relatively well estimated by both methods. The accuracy of both approaches is considerably less in the northern and central basins of Ecuador (0–3.6° S). It is shown that the detection probability is better for light precipitation (less than 5 mm day^{-1}). Compared to its predecessor 3B42V7 shows modest basin-wide improvements in reducing biases. The improvement is specific to the coastal and open ocean sub-catchments. In view of hydrological applications, the correlation of TMPA's and OA-NOSA30 estimates with observations increases with time aggregation. The correlation is higher for the monthly time aggregation in comparison with the daily, weekly and 15-daily time scales. Furthermore, it is found that TMPA performs better than OA-NOSA30 in generating the spatial distribution of mean annual precipitation.

1 Introduction

Precipitation is the primary driver of the hydrologic cycle and the main input of most hydrologic studies. Accurate estimation of precipitation is therefore essential. The availability of rainfall data, in particular in developing countries, is hampered by the scarcity of accurate high-resolution precipitation. Since its inception, rainfall measurements

HESSD
11, 411–449, 2014

principles remained unchanged; non-recording and recording rain gauges are still the standard equipment for measuring precipitation notwithstanding that they only provide point measurements. Rainfall amounts measured at different locations are traditionally extrapolated to give an areal average of rainfall. Errors in the point measurements of rainfall, in the order of 10 to 20 %, and a 10–20 % error in extrapolating data from a point measurement to an areal average, results to a considerable uncertainty in areal precipitation estimates (Willems and Berlamont, 2002). Areal rainfall estimates from point gauge measurements will only improve, if over time the rain gauge network density increases. One potential way to overcome the limitations of rain gauge based networks and weather radar systems in estimating areal rainfall is by using satellite-based global climate information and Numerical Weather Prediction (NWP), based on current weather conditions. To improve the accuracy of satellite rainfall estimation and NWP models, and facilitate their application; the evaluation of both products needs to be region specific and user-oriented.

A wide range of satellite derived precipitation products emerged the last decade and their performance over different regions of the world has been evaluated. Several studies have been conducted to assess the accuracy of three of the most widely used satellite based methods producing global precipitation estimates, such as the Climate Prediction Centre morphing method (CMORPH), Precipitation Estimation from Remotely Sensed Information Using Neural Networks (PERSIANN) and the Tropical Rainfall Measuring Mission (TRMM) Multisatellite Precipitation Analysis (TMPA) 3B42 (Romilly and Gebremichael, 2011). TMPA 3B42V6 version performance has been evaluated over the tropical Andes of South America at high-altitude regions (> 3000 m a.s.l.) by Scheel et al. (2011) with focus on the Cuzco and La Paz regions in the Central Andes. Ward et al. (2011) conducted similar investigation in the Paute region (> 1684 m a.s.l.) situated in the southern Ecuadorian Andes and Arias-Hidalgo et al. (2013) explored its applicability as input for hydrologic studies on a catchment in the Pacific-Andean basin in central Ecuador. They all concluded that disregarding the limitations at small temporal scale (daily) the performance of this product increases with time

HESSD
11, 411–449, 2014

aggregation and highlighted the potential to use TMPA 3B42V6 at large-scale basins. Dinku et al. (2010) conducted a wider evaluation covering different climatological regions and altitudinal ranges of the Colombian territory. Results showed good performance when the temporal scale increases (10 days), however they are region distinct yielding the best performance over the eastern Colombian plain below 500 m in elevation. The availability of the evolved version, the TMPA 3B42V7, opens a new question concerning its usefulness on South-American regions. Recently, Zulkafli et al. (2013) assessed the improvement of the V7 over the V6 and reported a lower bias and an improved representation of the rainfall distribution over the northern Peruvian Andes and the Amazon watershed. The diversity of South-American environments demands new comparisons over regions with different precipitation regimens and mechanisms.

On the other hand, NWP models capabilities keep evolving and providing precipitation fields at high spatio-temporal resolutions. In general, NWP models are not only valuable tools for weather forecasting but also for climate reconstruction. NWP can be initialized and bounded by assimilated observational data describing the large-scale atmospheric conditions throughout the reconstructed period. Periods of years to decades can be retrieved using NWP models, commonly known as "regional atmospheric reanalysis". Although, this technique is still in its early stages, in tropical South America, some NWP model applications were conducted by Muñoz et al. (2010). Their study follows a three-level hierarchical approach. Global-scale analysis and/or GCM outputs are generated and then used as boundary conditions for the meso-scale meteorological models, which in turn provide information for tailored applications. In a "regional atmospheric reanalysis" setting, the Weather Research and Forecasting model (WRF, Skamarock et al., 2005) was forced by applying boundary conditions of the NCEP/NCAR Reanalysis project (NNRP, Kistler et al., 2001) to retrieve for the first time meteorological data for North Western South America in the so-called OA-NOSA30 product. The aim of the retrospective simulation was to provide input data for hydrologic and health-epidemiological models with the hypothesis that the WRF retrospective simulation may

HESSD
11, 411–449, 2014

add skill to GCMs in countries where the Andes Mountain chain provides complex disturbances that global models cannot solve.

The westernmost N-S axis of South America, which embraces the Pacific-Andean basin of Ecuador and northern Peru (PAEP), is a region with below average density and unevenly distribution of meteorological stations. Because of its location, contrasting landscapes and complex topography, that includes humid regions of the western Andean foothills and arid areas offshore the coastal line, it provides a unique case to evaluate the potentials and drawbacks of satellite and numerical model rainfall estimates. In consequence, the objective of this study is to provide an evaluation of the performance of the TMPA V7 and its predecessor the TMPAV6 version and the OA-NOSA30 products versus regionalized ground data over the PAEP region. Specifically, emphasis is given to determine whether there are regions and time aggregation scales on which precipitation estimates may be considered as an alternative and/or complementary information source for poorly gauged basins.

2 Materials and methods

2.1 Study area

The western coast of South America is a region with contrasting landscapes and a rather complex orography. Near to the equator the coastal area of Ecuador is drenched with rainfall and supports dense vegetation down to the shore. However, at the southern margin and along the northern Peruvian littoral, the coast is stark and almost devoid of vegetation. The PAEP region (ca. 100 800 km^2) is located in the N-S axis between 0°–6° S and drains the westernmost slope of the Andes Cordillera (Fig. 1a). The various steep Andean ridges down to the coast together with the Cordillera "Costanera" shapes thirteen Pacific-Andean valleys from north to south: Chone (1), Portoviejo (2), Guayas (3), Taura (4), Cañar (5), Naranjal-Pagua (6), Jubones (7), Santa Rosa (8), Arenillas (9), Zarumilla (10), Puyango-Tumbes (11), Catamayo-Chira (12), and Piura

HESSD
11, 411–449, 2014

(13) (Fig. 1b) each one with particular geomorphological and climatological features. The proximity of the Andean mountain ranges to the coastal line is the main influence on the basin's relief and climatology. Short and steep basins, i.e. Puyango (10), descend from nearly 4000 m of altitude in less than 240 km of river length. On the other hand, large basins host the largest plains and low land valleys in the Ecuadorian littoral with roughly 70 % of its area below an elevation of 200 m. The Guayas (3), which is one the most important fluvial system in the western coast of South America, is such large basin.

2.2 Climate

The coastal region of Ecuador has a seasonal rainfall distribution characterized by a single rainy period, with 75–90 % of the rainfall occurring between December and May. Overall, in the PAEP region the rainy season starts around late November and ends in June, with a peak between February and March. Over the humid Andean foothills in the coastal plain a 2–3 month dry period separates the rainy seasons. On top of this seasonal rainfall pattern the distribution of precipitation is affected by the seasonal latitudinal migration of the Inter-Tropical Convergence Zone (ITCZ) and eastern tropical Pacific Sea Surface Temperature (SST) variations. The north-southern seasonal ITCZ displacement and SST variations bring to the area air masses of different humidity and temperature. When the ITCZ and the equatorial front are in their southernmost position near the equator, Ecuador's coastal regions are under the influence of warm moist air masses, originating from the northwest, bringing significant rainfall and rising air temperatures. The latter mainly defines the rainy season. Inversely, the northernmost ITCZ displacement and the equatorial front result in the presence of cooler and dryer air masses descending from upwelling regions in the south-west, influencing the dry season (Rossel and Cadier, 2009).

The most important feature of the rainfall variability in the PAEP region is the occurrence of inter-annual anomalies as related to the large-scale circulation phenomena such as El Niño-Southern Oscillation (ENSO). The PAEP region is bounded by the

HESSD
11, 411–449, 2014

limit of the strong ENSO influence defined by Rossel et al. (1999) as the region where the increase in mean annual precipitation is greater than 40 %. Therefore, in ENSO years abrupt changes in the mean annual rainfall conditions are considerable with a coefficient of variation reaching 0.40 (Rossel and Cadier, 2009). Such increase is not uniform basin-wide, there are important regional differences in heavy rainfall formation during El Niño (EN) events (Bendix and Bendix, 2006) and the EN influence on rainfall variability may change substantially in short distances in the same Pacific-Andean hydrological unit (Pineda et al., 2013). Futhermore, since 2000 an atypical meteorological response to EN and La Niña (LN) conditions is reported over the coastal plains and the western Andean highlands (Bendix et al., 2011). All together result into a very complex spatio-temporal distribution of rainfall patterns during ENSO and non ENSO years. These considerations are of paramount interest when dealing with data quality control of unevenly distributed rain gauges in the PAEP region.

2.3 Data

2.3.1 Rain gauge data

A ground precipitation network of 131 rain gauges with daily data (~ 1964–2010) in the PAEP region was provided by the Ecuadorian and Peruvian Meteorological and Hydrological Services, INAMHI and SENAMHI, respectively (Fig. 1b). Records with missing gaps higher than 20 % were deleted resulting in 107 time series of daily rainfall.

In a first step, a regionalization analysis was conducted to group spatially homogenous stations. The most reliable records were identified by selecting records with no changes in location and instrument type and then set as reference stations for a double mass analysis (Wilson, 1983). In the double mass analysis, the hierarchical criteria to check proportionality in the cumulative monthly volumes between the reference and the candidate station involves: (i) neighbouring, (ii) altitude range, and (iii) exposure to the same meso/synoptic climatological feature (e.g. ENSO).

HESSD
11, 411–449, 2014

Following, the temporal homogeneity of each record was checked against error measurements so that variations are attributed only to climate processes. The R-based RHtests_dlyPrcp software package, developed by the Climate Research Division of the Meteorological Service of Canada and which is available from the Expert Team on Climate Change Detection, Monitoring and Indices (ETCCDMI) website (Wang and Feng, 2012), was used to identify multiple step changes at documented or undocumented change points (shifts in the mean). It is based on the integration of a Box-Cox power transformation into a common trend two-phase regression model suitable for non-Gaussians series such as non-zero daily precipitation (Wang et al., 2010). Documented changes (EN driven) are referred as those defined by Rossel and Cadier (2009) and are the sequence of at least three consecutive months where the monthly SST anomalies are above 23 °C and exhibit a positive anomaly equal or greater than 1 °C. Such events occurred in the years 1965, 1972–1973, 1976, 1982–1983, 1987, 1992 and 1997–1998. For LN driven-changes the year 2008 was also considered. Non-homogeneous periods were considered as modifications in the field during data collection and set as Not Available (NA) and then retested to verify whether they are homogeneous with the disregarded period(s).

2.3.2 TMPA TRMM 3B42 products

TMPA precipitation products are available in two versions: near-real-time version (3B42RT) and post-real-time research version (3B42) calibrated and merged with monthly rain gauge data. The 3B42 products have two successive versions: version 6 which computation ended as June 2011 and the latest version 7.

The TMPA 3B42V6 consists of hourly rainfall rates ($mm\,h^{-1}$) at surface level with a global coverage between 50° N and S since 1998. This method combined precipitation estimates of four passive microwave (PMW) sensors, namely TRMM Microwave Imager (TMI), Special Sensor Microwave/Imager (SSM/I) F13, F14 and F15, Advanced Microwave Scanning Radiometer-EOS (AMSR-E) and Advanced Microwave Sounding Unit-B (AMSU-B). The TMPA V6 algorithm is described in Huffman et al. (2007).

HESSD
11, 411–449, 2014

The improved version, the 3B42 V7, includes consistently reprocessed versions for the data sources used in 3B42V6 and introduces additional datasets, including the Special Sensor Microwave Imager/Sounder (SSMIS) F16-17 and Microwave Humidity Sounder (MHS) (N18 and N19) and Meteorological Operational satellite programme (MetOp) and the 0.07° Grisat-B1 infrared data. The changes in the V7 algorithm at various processing levels are described in Huffman et al. (2010) and Huffman and Bolvin (2012). TMPA 3B42V6 and 3B42V7 precipitation estimates in 3-hourly, 0.25 × 0.25 degrees resolution were aggregated to daily data for the 1998–2008 11 yr period.

2.3.3 WRF retrospective simulation

The Scientific Modelling Centre from Venezuela (CMC) and the National Institute of Hydrology and Meteorology from Ecuador (INAMHI) developed a North Western South America Retrospective simulation. The dataset, called OA-NOSA30, is available online at the International Research Institute for Climate and Society (IRI) web page (Muñoz and Recalde, 2010). The simulation provides numerous climate variables with a 30 km spatial and 6 h temporal resolution and a global coverage between 11° S to 17° N and 98° W to 50° E. The accumulated precipitation was extracted on a daily basis for the period January 1998 to December 2008, enabling comparison with the TMPA and rain gauge data.

OA-NOSA30 is the simulation result from the Weather Research and Forecasting (WRF) model, a Regional Climate Model (RCM) herein used to downscale the meteorological data from the NCEP/NCAR Reanalysis Project (NNRP or R1, details at Kistler et al., 2001). NNRP stands for the combination of global climate model outputs and observations. The WRF configuration for the Microphysics Parameterization, governing the outputs, was applied. Muñoz and Recalde (2010) explained that the microphysics were modelled by the Kessler scheme (RRTM), the Dudhia schemes were used for the modelling of the longwave and shortwave radiation, respectively; the Monin-Obukhov (Janjic) scheme for modelling of the surface-layer; and the thermal diffusion with 5 soil levels for modelling the land-surface physics. Finally the Mellor-Yamada-Janjic TKE

HESSD
11, 411–449, 2014

scheme was applied for describing the boundary-layer option, in which the SST update option was selected.

2.4 Gridded rainfall dataset

The appropriate scale to use spatially averaged precipitation products should be large enough to reduce random errors but retain topographical gradients (Bell and Kundu, 2003), therefore we search for a trade-off by comparing basin station-gridded precipitation fields against basin averaged precipitation products. Rather than rescaling the products to an arbitrary resolution the products were evaluated at sub-catchment scale identified during the regionalization analysis. Namely, instead of a punctual comparison, spatial averages were calculated for the precipitation products using the proportional coverage of each grid cell. All data-quality checked records were interpolated to obtain spatial averages in each sub-catchment, except the few whose data is available through the Global Telecommunication System (GTS). Data from these stations may have been used for adjusting TRMM estimates. Thus, these stations (03) were excluded from the interpolation.

Using the kriging approach for the spatial interpolation of daily rainfall over complex terrains, the incorporation of correlation with topography/altitude has been suggested to improve performance; see Buytaert et al. (2006) for highlands ~ 3500 m a.s.l. and Cedeño and Cornejo (2008) for the coastal region below 1350 m a.s.l. in Ecuador. In a climatological study for Ecuador and North Peru, Bendix and Bendix (1998) showed that the inclusion of the altitude increases significantly the correlation between observed and interpolated values. Also, Rollenbeck and Bendix (2011) applied the kriging technique with altitude as an external variable, in southern Ecuador, for the interpolation of INAMHI precipitation data in a 120 km by 120 km grid for the calibration of rainfall data obtained from a cost-efficient mini-radar station.

Parallel, several interpolation techniques of increasing complexity have been developed and evaluated using the gstat R package (Edzer Pebesma, 2011). Inverse distance weighting (IDW) and original kriging (OK) are fairly similar; both take into account

HESSD
11, 411–449, 2014

the distance between stations, but OK has a more complex formulation and therefore expected to be more accurate. Linear regression (LR) is supposed to perform similar to kriging with external drift (KED) since they both implement regression with altitude. KED is, however, more accurate accounting for kriging of residuals, which means that distance between stations influences interpolation as well. To discern among different interpolation techniques Li and Heap (2008) recommends assessing the performance by cross validation methods.

A key issue in this study is whether the change of spatial support provides a sound reference for comparison with TMPA's and WRF products. It is often the case in Pacific-Andean landscapes that high elevation areas are under-sampled in comparison to lowlands valleys, which may introduce biases in the interpolation. While the cross validation analysis provides residuals variance to address uncertainty among interpolation techniques, it is acknowledged that kriging variance is not a true estimate of uncertainty (Yamamoto, 2000; Haylock et al., 2008). In general, errors and uncertainty in a gridded dataset arise from many sources, including errors in the different steps of the data supply chain (measurements, collection, homogeneity) and in the interpolation technique. It would be ideal to split and quantify all of them. This is, however, not possible without the possibility to track them back. A solution would be to perform an ensemble of stochastic simulations from which uncertainty can be estimated at the expense of highly computational resources. Such detailed analysis is out of the scope of this work. We therefore quantify the total residual variance and split it up in its main contributing residual variance sources (input (data) and kriging interpolation (geo-statistical model)) based on a variance decomposition technique (Willems, 2008, 2012) in order to estimate the fraction of each contributing source. The total residual variance is assessed based on statistical analysis of the residuals between each precipitation product ($Y_{\mathrm{TRMM/OANOSA30}}$) and KED estimates ($Y_{\mathrm{KED}}$). The underlying assumption of the variance decomposition is that the (causes of the) errors on the $Y_{\mathrm{TRMM/OANOSA30}}$ and Y_{KED} precipitation estimates are highly different, hence that they can be assumed independent. The residuals are converted into homoscedastic

HESSD
11, 411–449, 2014

residuals by means of a Box-Cox (BC) transformation (Box and Cox, 1964). After this conversion, the total $Y_{\text{TRMM/OANOSA30}}$ residual variance ($S^2_{\text{BC(YTRMM/OANOSA30,Residual)}}$) is decomposed into the precipitation product error variance, hereafter called model error variance ($S^2_{\text{BC(YTRMM/OANOSA30,Model)}}$), and the KED error variance ($S^2_{\text{BC(KED)}}$) (Eq. 1). The KED uncertainty is evaluated using just the random field provided by a single realization with prescribed parameters (i.e. mean structure, residual variogram) (Yamamoto, 2000). We estimate the total ($Y_{\text{TRMM/OANOSA30}}$) residual variance at every tile ($_{\text{TRMM/OANOSA30-KED}}$). By subtracting the KED error variance from the total residual variance of $Y_{\text{TRMM/OANOSA30}}$ based on Eq. (1), we obtain indirect estimates of the model error variance and map its spatial distribution.

$$S^2_{\text{BC(YTRMM/OANOSA30,Residual)}} = S^2_{\text{BC(YTRMM/OANOSA30,Model)}} + S^2_{\text{BC(KED)}} \quad (1)$$

2.5 Products evaluation

Bias, root mean square error (RMSE) and Pearson's correlation (γ_{xy}) were applied to analyse the accuracy of the TMPA's and OA-NOSA30 estimates comparing them with rain-gauge interpolated estimates at sub-catchment scale (Eqs. 1 to 3). RMSE includes both systematic (bias) and non-systematic (random) errors.

$$\text{BIAS} = \frac{1}{n}\sum_{i=1}^{n}(P^{\text{pp}}_{xi} - P^{\text{gauge}}_{xi}) \quad (2)$$

$$\text{RMSE} = \sqrt{\frac{1}{n}\sum_{i=1}^{n}(P^{\text{pp}}_{Xi} - P^{\text{gauge}}_{Xi})^2} \quad (3)$$

$$\gamma_{xy} = \frac{\text{Cov}(P^{\text{PP}}, P^{\text{gauge}})}{\sqrt{\text{Var}(P^{\text{pp}})} \times \sqrt{\text{Var}(P^{\text{gauge}})}} \quad (4)$$

HESSD
11, 411–449, 2014

Where, P^{pp} is the precipitation products value, P^{gauge} the interpolation estimate from rain gauge values, and n the number of observations.

Additionally, skill scores were calculated to quantify the products accuracy in detecting daily accumulation at different precipitation thresholds and they were calculated based on average sub-catchment precipitation. The Probability of Detection (POD) gives the fraction of rain occurrences that were correctly detected; it ranges from 0 to a perfect score of 1. The Equitable Threat Score (ETS) measures the fraction of observed and/or detected rain that was correctly detected and adjusted for the number of hits that could be expected due purely to random chance. A perfect score for the ETS is 1. The Frequency Bias Index (FBI) is the ratio of the number of estimated to observed rain events; it can indicate whether there is a tendency to underestimate or overestimate rainy events. It ranges from 0 to infinity with a perfect score of 1. The False Alarm Rate (FAR) measures the fraction of rain detections that were actually false alarms. It ranges from 0 to 1 with a perfect score of 0 (Su et al., 2008).

The ETS is commonly used as an overall skill measure by the numerical weather prediction community, whereas the FBI, FAR, and POD provide complementary information about bias, false alarms, and misses. To evaluate the performance of the products for light and heavy precipitation events they were calculated for each sub-catchment and for several thresholds: 0.1, 0.5, 1, 2, 5, 10, and 20 mm day^{-1} (Schaefer, 1990; Su et al., 2008).

Seasonality accuracy at sub-catchment level was evaluated confronting precipitation estimates with interpolated average monthly rainfall depths. Furthermore, in order to evaluate precipitation products on increasing time scales, daily, weekly, 15-daily and monthly estimates were accumulated finding Pearson's correlation (Eq. 3) and bias in percentage. Bias from Eq. (1) was modified by getting rid of the units, thus finding the quotient of precipitation products bias by the observed precipitation value per day/week/15 days/month and averaging the results for the whole time series in order to compare different time aggregations. Finally, annual mean precipitation was calculated for interpolated rain gauges and precipitation products and depicted spatially.

HESSD
11, 411–449, 2014

3 Results

3.1 Data quality verification, interpolation and uncertainty

The double mass analysis discriminated 21 sub-catchments within which rainfall is spatially correlated. The proportionality is strong in the coastal areas where the altitude range is narrow, but is less marked at higher altitudes making the grouping evasive. Four stations do not have significant correlation with any other station, and the sub-catchments in which they are situated were ranked as independent.

The temporal homogeneity check for each station reported several change-points, with a statistical significance of 5 %. However, most of them were attributed to EN regional variations and therefore rejected as artificial change-points. Besides the documented changes, several change-points appeared repeatedly in nearby locations. They were interpreted as a common modification in the local climate and therefore disregarded as change-points. Despite of these considerations, non-homogeneous periods significant at 5 % were found in 30 stations. Those periods were discarded and the stations tested again for homogeneity. Nine stations did not pass the test. Therefore they were no longer taken into account, resulting into a quality checked set of 98 time series. From this dataset the 11 yr period, January 1998 to December 2008, was taken for the comparison between OA-NOSA30 and the TMPA's estimates, and rain gauge precipitation data. The 98 homogeneous stations together with the 21 homogenous sub-catchments are shown in Fig. 1b. The area and the density of the rain gauge stations per sub-catchment are listed in Table 1. The highest density is found in Quiroz, Upper Guayas, Alamor, Chipillico and the lowest in Naranjal-Pagua, Lower Guayas and Piura and Tumbes.

Table 2 reports the mean cross validation results of the four investigated techniques to grid daily precipitation in the period 1998–2008. Correlation for KED (0.49) is twice the value than for IDW, LR, and OK techniques (0.26, 0.28, and 0.21, respectively). Not only its mean is higher but correlation on almost every day was better than for any other technique. Table 2 shows that KED outperform other techniques. The Mean

HESSD
11, 411–449, 2014

Square Error (MSE) for KED is less than for LR and slightly less for OK. The performance values explain how good the technique represents the variability of the precipitation assessed by the squared of the residuals and it was found better for KED. In general, KED performed better and LR was the second best. Foregoing confirms that taking into account altitude as a variable improves the interpolation of rainfall fields, as shown by Bendix and Bendix (1998) in the same area. Finally, the KED technique, which includes variogram analysis and the use of a 92 × 92 m Digital Elevation Model (DEM) from the Shuttle Radar Topography Mission (SRTM) as external drift, was chosen to interpolate station precipitation. The result is a daily gridded dataset (4018 time steps) with 92 × 92 m resolution, for which we believe it captures the horizontal and vertical gradients as well as the most prominent orographic effects. Its constraints and uncertainty is discussed prior to the next level of analysis.

Figure 2a, b and c presents results of the uncertainty analysis for the comparison of OA-NOSA30, TMPAV6 and V7 with KED estimates, based on the variance decomposition technique of one-day single random realization. Figure 2a shows that the OA-NOSA30 estimates are subject to the largest model residual variance, which strongly correlates with the high topographic precipitation gradients as seen over the inner-sierra foothills (i.e. Upper-Guayas (5), Cañar (7) and Jubones (9)), and to a lesser extent over the moderate slopes of the Cordillera Costanera (i.e. Chone (1)). The KED uncertainty has the highest contribution to the total residual variance in these regions whereas in the remaining stations the contribution of the KED uncertainty is more or less proportional to the total residual variance. In the comparison of TMPAV6-V7 (Fig. 2b and c) with KED estimates the spatial trends are less evident. Correlation with elevation still takes place in the V6 analysis but the large total residual variance does not show clear distinction between middle (∼ 500 m a.s.l.) and high altitudes (∼ 3000 m a.s.l.). For the V7 analysis the uncertainty mapping shows a more scattered distribution with almost no spatial trends. In both the V6 and V7 cases, the KED contribution to the total uncertainty remains slightly larger than the precipitation product error variance. All results together suggests that when comparing precipitation

HESSD
11, 411–449, 2014

products against KED estimates, the TMPAV7 based product, in the first place, followed by the V6 product, offer the best precipitation estimates since the precipitation uncertainty is less affected by the topographic setting that provides the basis for our proposed gridded dataset. The largest errors are encountered in the comparison between OA-NOSA30 and KED estimates at high altitudes, which have implications to our catchment-averaged analysis. These limitations are born in mind when interpreting the results in the next sections.

3.2 Daily verification

Figure 3a, b, c shows the bias, RMSE and Pearson's correlation between precipitation products and daily KED estimates accumulated over each sub-catchment unit and ranked from N-S within the period 1998–2008. These statistics reveal a strong spatial variation; for 3B42V6 and OA-NOSA30 bias and RMSE decrease from North to South while correlation increases, whereas for TMPA V7 significant bias reduction and increase in correlation seems sub-catchment and precipitation regimen dependent.

TMPA V7 and V6 overestimate precipitation in all sub-catchments, with an average range between 0 to $\sim 2\,\mathrm{mm\,day^{-1}}$. Conversely, OA-NOSA30 underestimates precipitation, except in Quiroz (17) and Chipillico (19), the range of over/under estimation is within ~ 0.5 to $-1.5\,\mathrm{mm\,day^{-1}}$ (Fig. 3a). The RMSE ranges from 4 to $9\,\mathrm{mm\,day^{-1}}$ for both TMPA estimates. The RMSE gives more weight to the extremes because residuals are squared and they are typically higher for precipitation extremes. Given that, particularly for TMPA V6, the bias is very high in wet seasons RMSE values are higher for TMPA V6 estimates than for OA-NOSA30 (Fig. 3b).

Figure 3c illustrates the N-S variability of the Pearson correlation. Pearson correlation is very similar between TMPA V6 and OA-NOSA30 oscillating between 0.3 and 0.6 except in Arenillas (11) where OA-NOSA30's detection fails. In the Northern region the highest correlation (0.5) is found at Lower/Middle Guayas (3)/(4) and the rest of the northern sub-catchments record correlations ~ 0.3. In the Central region, average correlation is about 0.35. In the southern region, correlation consistently rises to 0.5 in

HESSD
11, 411–449, 2014

a large area (Catamayo-Chira and Piura catchments). TMPA V7 shows a very modest basin-wide improvement over TMPA V6 only with a notorious correlation increase on Chone (1), Upper Guayas (5), Taura (6), Jubones (9) and Zarumilla (12).

Furthermore, when calculating bias by applying upper thresholds to the precipitation amounts (0.1, 0.5, 1, 2, 5, 10, and 20 mm day^{-1}) it is found that both TMPA's and OA-NOSA30 better detect small precipitation rates (data not shown). OA-NOSA30 presents almost no basin-wide bias on precipitation rates less than 1 mm day^{-1}. For the southern sub-catchment: Alamor (15), Macará (16), Quiroz (17), Chira (18) and Piura (21) this is the case up to 10 mm day^{-1}; over such a threshold precipitation is systematically underestimated. TMPA V7 and V6 overestimate precipitation amounts smaller than 10 mm day^{-1} in sub-catchments in the central and southern regions. For lowland areas in the north this threshold changes to 20 mm day^{-1}. As well as for OA-NOSA30, precipitations over 20 mm day^{-1} are systematically underestimated.

Figure 4a, b and c shows categorical scores POD, ETS, FBI and FAR for representative sub-catchments distributed in the Northern, Central and Southern region corresponding to the TMPA V7, V6 and OA-NOSA30 estimates. The four sub-catchments shown in Fig. 3 were chosen as representative according to their location and dominant precipitation regime. In the humid northern part, Chone (1), a coastal and ocean exposed sub-catchment, and Middle Guayas (4) in the inner core and greatly influenced by the continental climate divide, were selected. In the Central region, Jubones (9) with a pronounced leeward effect; and Chira (18) in the southern arid coast influenced by the "Sechura" desert, were considered. Their indexes lead to conclusions which can also describe the situation of the surrounding sub-catchments in each region. The difference between scores of TMPA V7 (4a) and V6 (4b) is almost undistinguished, both estimates shows a POD value of 0.6, on average, for precipitation rates less than 5 mm day^{-1}. It gradually decreases to $\sim$ 0.2 when the threshold is higher than 20 mm day^{-1}. A close inspection reveals a marginal improvement of V7 over V6 only evident in Middle Guayas (4) at higher thresholds. ETS scores, for precipitation estimates equal or lower than 5 mm day^{-1}, are on average 0.25. ETS, a summary score

HESSD
11, 411–449, 2014

that penalizes for hits that could occur due to randomness, can be use to compare performance across regimes. A slight improvement of V7 across all threshold is restricted to Chone (1). FAR and FBI curves show that the FBI increases with higher thresholds, as well as the FAR. This means that overestimation exists over 1 or 2 mm day^{-1} and false alarms are then also present. In general, TMPA's detects amounts of precipitation higher than 5 mm day^{-1} but it overestimates them; while amounts of precipitation less than 2 mm day^{-1} are detected with a low fraction of FAR, although bias is present. TMPA's scores are better in the Southern region, Chira (1), (higher ETS, FBI around 1, and smaller FAR values).

Figure 4c show the same categorical scores for OA-NOSA30. In all sub-catchment, POD decreases when the threshold increases, indicating that the NWP estimates better small precipitation events. POD decreases abruptly to 0 when considering thresholds of 5 and 10 mm day^{-1} thresholds. The behaviour of ETS scores is the same as for POD but the average scores are half the amount of POD. For small amounts of precipitation, i.e. less than 3 mm day^{-1}, OA-NOSA30's POD scores are around 0.6 while ETS scores are 0.3. The FBI plot shows underestimation, almost all values are less than 1. False alarms increase with higher thresholds with FAR values typically in the range 0.2 to 0.5. There are no FAR values given for thresholds over 5–10 mm day^{-1} since the POD of OA-NOSA30 is zero for those precipitation depths. Spatially, POD and ETS show a better probability of detection in the Southern region and FBI shows lower bias in that region compared to the Northern and Central regions; however FAR is lower in the Northern region Middle Guayas (4).

3.3 Monthly verification

Although Fig. 5a, b and c shows the mean monthly precipitation within the period 1998–2008 for KED estimates against TMPA V7, V6 and OA-NOSA30 for the four selected sub-catchments, the analysis below corresponds to all 21 sub-catchments. In general, Fig. 5c reveals that the three approaches yield comparable results for the Southern region, which includes the sub-catchments Alamor (15), Macará (16), Quiroz (17), Chira

HESSD
11, 411–449, 2014

(18), and Chipillico (19). In most of the sub-catchments, all datasets depict well seasonality showing wet conditions within the period January-May. In the Northern and Central regions, during the wet season, TMPA V7 and V6 overestimate while OA-NOSA30 underestimates precipitation (Fig. 5a, b). The pattern of over- and underestimation is not that clear in all datasets during the dry season. Maussion et al. (2011) showed that the WRF and TRMM well estimated the precipitation distribution, but depths and positions of maxima do not match. Additionally, they showed that WRF usually predicts more rainfall over larger areas, notwithstanding WRF may be closer to reality than TRMM. Furthermore, their results clearly illustrated that neither point measurements nor coarse grids can properly depict the spatially varying precipitation patterns, especially in mountainous terrains.

The density of rain gauges in the Catamayo-Chira catchment is higher and also the quality of data is better (fewer missing gaps and change-points). This might indicate that KED estimates are better for this area. However, in most of the Southern region TMPA and OA-NOSA30 estimates are similar to KED estimates even on high altitude sub-catchment i.e. Quiroz (17), which is not the case for the rest of the sub-catchments. Also, there are other sub-catchments such as Catamayo (14) and Upper Guayas (5) where the precipitation estimates are neither similar between them nor to KED estimates, despite the high quality of data. Thus, KED estimates prove to be a good reference and the dependence of the interpolation technique on the rain-gauge density as well as the error seen at high altitudes when comparing OA-NOS30 and KED is not affecting substantially the analysis. This is a very important issue, given that the density of rain gauges is relatively low and building up a gridded rainfall dataset that is the least influenced by this fact is crucial. TMPA's overestimation occurs for any precipitation amount when aggregated per month (Fig. 5); unlike daily aggregation where over-underestimation occurs according to the amount of precipitation (see FBI scores in the Fig. 4a and b).

HESSD
11, 411–449, 2014

3.4 Verification on multi-temporal resolutions

The Pearson correlation (Fig. 6a) and bias (Fig. 6b) were calculated on daily, weekly, 15-daily and monthly time scales for TMPAV7, V6 and OA-NOSA30. In general, they have equal tendency although bias and correlation values are different. Correlation increases with time scale, and is higher for monthly than 15-daily and weekly time aggregated periods. Bias seems to accumulate when time aggregation increases as found in other regions (Cheng and Steenburgh, 2005; Ruiz et al., 2010). The purpose of finding the bias in the estimates is to quantify respectively the over-underestimation of the precipitation depth, which is higher when time aggregation increases. The bias percentage is consistent with the correlation coefficient, decreasing substantially as the time aggregation increases. Although the daily bias is high in Jubones (9) ($\sim 1000\,\%$ for V7 and $\sim 1200\,\%$ for V6) and surprisingly in Middle Guayas (4), higher for V7 than V6; on a weekly to monthly scale the bias percentage decreases. The worst performance of both TMPA estimates was found in Jubones, where less correlation and a higher bias percentage is evident. For OA-NOSA30 that is the case for Chone (1) and Jubones (9). The results found for TMPA, i.e. the correlation increases and bias reduces as time aggregation increases, are in agreement with previous studies (Scheel et al., 2011; Habib et al., 2009; among others).

Aggregation of the mean annual rainfall was performed to illustrate and compare the spatial performance of the three approaches (OA-NOSA30, TMPAV6 and V7) against KED estimate in the study area (Fig. 7). Comparison shows that the TMPA estimates are close to the spatial variation of the mean annual rainfall, although mean annual rainfall in the north and south-east are overestimated. OA-NOSA30 presents a huge underestimation and does not reflect spatial variability, with the exception of the Southern region. Here OA-NOSA30 bias is small enough to represent a spatial precipitation pattern approaching the spatial pattern based on TMPA estimates.

HESSD
11, 411–449, 2014

4 Discussion

TMPA V7 and V6 estimates show different basin-wide skills on daily basis but they yield comparable results particularly in the Southern region (3.6–6° S) in weekly to monthly time aggregations. TMPA V7 shows localized higher skills than V6 on short-steep costal and ocean exposed sub-catchments but lower skills on large inland basins. Whether this improvement/detriment is specific to a precipitation regime and is related to the changes incorporated in the newer version is discussed at end of this section. We firstly focus on issues regarding rainfall retrieval which are common to both versions.

Our analysis reports that both TMPA products overestimate precipitation in the 21-subcatchments of the heterogeneous PAEP region. Key challenges in the estimation of precipitation from satellite estimates arise from the processing scheme for MW and IR data. The problem with IR data processing is that global algorithms do not consider the altitude of the hydrometeor. Dinku et al. (2011) suggest that overestimation over dry areas may be attributed to sub-cloud evaporation. While this mechanism may have implications on the overestimation of TMPA onshore the coastal plain, especially in the arid Peruvian littoral where a dry low-atmosphere is common all year-round; the attribution of TMPA overestimation to sub-cloud evaporation on the middle/high altitude sub-catchments is inconclusive. Bendix et al. (2006) showed that, over the Ecuadorian territory and surroundings, average cloud-top height increase from W-E showing a more stratiform cloud dynamics in the Pacific area and the coastal plains, and, that the western Cordillera is a true division for the Pacific influence. They describe the seasonal spatial pattern of cloud-top height distribution within December-May (wet season), possessing a well-defined blocking height ($\sim 4.5 < 5.0$ km) between 0–3° S, but less marked southward. Given that TMPA algorithms estimate precipitation from the brightness temperature at the cloud top (implicitly cloud height) it would be expected that overestimation follows the same spatial pattern. However, our analysis showed that even though TMPA overestimation matches the increasing W-E cloud-top gradient it does not allow explaining the large overestimation in the Northern bottom valleys

HESSD
11, 411–449, 2014

(i.e. Lower Guayas and Chone catchment). The regional differences in cloud properties between the Northern and Southern catchments better explains the differences in TMPA overestimation. Over the northern region ∼0° (Quito-transect), see Bendix et al. (2006) for full details, cloud frequency is substantially higher in contrast to the reduced cloudiness at ∼4° S (Loja-transect). To illustrate these differences Fig. 8a, b, c show cloud density patterns using anomalies of interpolated Outgoing Longwave Radiation (OLR) (Liebmann and Smith, 1996) as proxy for cloudiness (negative anomalies imply increased cloudiness) during the rainy season within 1998–2008. During December-January (8a) symmetrical patterns of cloudiness are observed over northern and southern sub-catchment, increased cloudiness concentrate over the northwestern edge during January February (8b) which then exhibit a north-southeast gradient in April–May (8c). This suggests that in addition to the error introduced by the estimation of the cloud-top, the TMPA overestimation on the Northern catchments may also be influenced by the high occurrences of low stratiform clouds (typical on the coastal area) which under stable conditions are detached from precipitation patterns (Bendix et al., 2006). This high density of non-rain producing clouds would affect the IR data retrieval resulting into overestimation. The largest deficiencies of TMPA's estimates are encountered in separating the windward/leeward effect of the Andean ridges on orographic rainfall which is particularly witnessed in Jubones where the leeward effect is dominant. West of the climate divide there is not typical precipitation gradient. Through blocking at the ridges and through re-evaporation, rainfall of any origin affects more frequently higher elevations than valley floors (Emck, 2007). What is specific to the V7 product is the improvement on detection capacity of light orographic precipitation on coastal ocean exposed sub-catchments, where the spatial sampling seems to capture small precipitation gradients; over coastal areas orographic enhancement is a small spatial scale event (Minder et al., 2008; Cheng et al., 2013). In the inner-most sub-catchments where gradients on annual precipitation may reach i.e.700 mm/100 m at 3400 m a.s.l. (Emck, 2007) the temporal sampling of V7 cannot capture the rapid

HESSD
11, 411–449, 2014

evolution of orographic rainfall and the overestimation is similar to that of the V6 version.

OA-NOSA30 product only shows considerable skills in the Southern region (3.6–6° S) where amount and occurrence are considerable well represented. The greatest NWP limitations are encountered in representing the enhancement of convective rain rates due to the effect of the coastal mountains as premier barrier for moisture transport in short-steep coastal sub-catchments (3–3.6° S) where the nearly null detection capacity is explained by the unique rainfall rates that occur on the ocean facing foothills of the Cordillera "Costanera". Unlike in most tropical mountains where convective rainfall dominates in Southeast west Ecuador vigorous advection shape a monotonic increasing precipitation gradient with altitude. In the core of the southern region, Motilon station (04°05′ S, 79°56′ W, 2690 m a.s.l.), Emck (2007) reported that rainfall originates from an equal-balance of advective-topographic (light) and convective (heavier) genesis. Such a characteristic, probably particularly for the Southern region, suggests that the NWP parameterization for OA-NOSA30 is particularly suited to solve this type of precipitation. For the Northern regions, which are more affected for the annual spillover of the ITCZ, the influence of the continental climate divide and the occurrence of more stratiform cloud, deep convection (likely the dominant mechanism) is far from be emulated by the NWP model. A complete description of the errors in the NWP implementation is out of the scope of this study, we therefore only highlight some of the major sources. The lateral boundary conditions (NNRP dataset) have presumably a major role on the degradation of WRF product quality. The poor representation of the Andes in the reanalysis model has showed to contribute to a modest representation of meteorological fields such as wind (Schafer et al., 2003). Maussion et al. (2011) found that some undesired numerical effects and, eventually, inadequate input data can affect the operational output of the WRF model, in particular for extreme events; probably by overstressing certain physical processes. Jankov et al. (2005) found that the greatest variability in rainfall estimates from the WRF model originates from changes in the choice of the convective scheme, although notable impacts were observed from

HESSD
11, 411–449, 2014

changes in the microphysics and planetary boundary layer (PBL) schemes. However, Ruiz et al. (2010) found that rainfall estimates only vary slightly among different configurations, but biases increase with time aggregation. Those findings agree with previous studies (Blázquez and Nuñez, 2009; Pessacg, 2008) and suggest that there is a common deficiency in the convective schemes used in this and other investigations.

5 Conclusions

In general, TRMM V7, V6 and OA-NOSA30 estimates capture the most prominent seasonal features of precipitation in the study area. Quantitatively, only the Southern sub-catchments of Ecuador and Northern Peru are nearly equally estimated by both satellite and NWP estimates. There is low accuracy of both approaches in the Northern and Central regions where TMPA V7 and V6 overestimates while OA-NOSA30 systematically underestimates precipitation. The improvement of V7 over V6 is not evident basin-wide and appears inherent to detection of light precipitation rates on coastal and ocean exposed basins. Inland the differences of both estimates are almost unnoticeable. The separation of the windward/leeward Andean effect on orographic precipitation appears as the main challenge for TMPA algorithms. It was found that the detection probability is better for small rainfall depths, less than 5 mm day^{-1}, than for high amounts of precipitation. OA-NOSA30 showed acceptable skills in detecting a balanced advective/convective regimen of precipitation in the Southern region,

Analysis of daily, weekly, 15-daily and monthly time series revealed that the correlation with station observations increases and bias decreases with the time aggregation. Differences are considerably larger for daily than weekly aggregation. The correlation and bias values are similar in the Northern and Southern region but in the Central region correlation is smaller and bias is higher for all time aggregations. TMPA V7, V6 and OA-NOSA30 are able to capture relatively well the spatial pattern in the Southern region of the study area, but the performance of both approaches reduces in the Northern and Central region. In general TMPA's perform better than OA-NOSA30.

HESSD
11, 411–449, 2014

In view of hydrological and water resources management applications, it has been demonstrated that there is a potential to profit from both estimates in a particular region of Southern Ecuador-Northern Peru, at temporal scales larger than a week. This is relevant for meteorological operational forecasting and water budget studies in this poorly gauged region. At present, satellite products are used as the most important tools for forecasting within the next six hour (nowcasting) while the dynamical weather forecast systems are still in an experimental stage (in Ecuador). However, for hydrological applications such as flood warning, in which high temporal resolution, accurate depth and storm location is needed, the usefulness of both estimates is less promising.

Blending the precipitation estimates with interpolated estimates from rain gauge stations might be recommended, because inaccuracies typical for each approach might be compensated by their combination. Precipitation products are biased, but can be corrected with ground estimates. However, this merging procedure is not straightforward if done for operational purposes; this could be an area of fruitful research for the meteorological services of the region.

Acknowledgements. L. Pineda was funded by an EMECW grant of EC for doctoral studies in KU Leuven. A. Ochoa acknowledges VLIR-UOS for the scholarship, which enabled a study stay in Belgium during which most of the presented research was conducted. Gratitude is expressed to the National Services of Meteorology and Hydrology of Ecuador (Raúl Mejía, INAMHI) and Peru (Héctor Yauri, SENAMHI) for making the station data available. The authors thank D. Mora (PROMAS-Cuenca University) for assistance with geospatial information and Jan Feyen of Cuenca University for his valuable comments and suggestions to improve the manuscript.

References

Bell, T. L. and Kundu, P. K.: Comparing satellite rainfall estimates with rain gauge data: Optimal strategies suggested by a spectral model, J. Geophys. Res., 108, 4121, doi:10.1029/2002JD002641, 2003.

Bendix, J. and Bendix, A.: Climatological Aspects of the 19991/1993 El Niño in Ecuador, Bulletin de L'Institut Francaise d'Etudes Andines, 27, 655–666, http://lcrs.geographie.uni-marburg.de/fileadmin/media_lcrs/paper_bendix/BENDIX_BIFED98.PDF, 1998.

Bendix, A. and Bendix, J.: Heavy rainfall episodes in Ecuador during El Niño events and associated regional atmospheric circulation and SST patterns, Adv. Geosci., 6, 43–49, doi:10.5194/adgeo-6-43-2006, 2006.

Bendix, J., Rollenbeck, R., Gottlicher, D., and Cermank, J.: Cloud ocurrence and cloud properties in Ecuador, Clim. Res., 30, 133–147, 2006.

Bendix, J., Trachte, K., Palacios, E., Rollenbeck, R., Göttlicher, D., Nauss, T., and Bendix, A.: El Niño meets La Niña-Anomalous rainfall patterns in the "Traditional" El Niño region of southern Ecuador, Erdkunde, 151–167, 2011.

Blázquez, J. and Nuñez, M. N.: Sensitivity to convective parameterization in the WRF regional model in southern South America, in: Ninth Int. Conf. on Southern Hemisphere Meteorology and, Oceanography, Melbourne, Australia, Am. Meteorol. Soc., 6 pp., 2009.

Buytaert, W., Celleri, R., Willems, P.,De Bièvre, B., and Wyseure, G.: Spatial and temporal rainfall variability in mountainous areas: A case study from the south Ecuadorian Andes, J. Hydrol., 329, 413–421, doi:10.1016/j.jhydrol.2006.02.031, 2006.

Cedeño, J. and Cornejo, M. P.: Evaluation of three precipitation products on ecuadorian coast, available at: http://wcrp.ipsl.jussieu.fr/Workshops/Reanalysis2008/Documents/Posters/P3-25_ea.pdf (last access: 12 April 2012), 2008.

Cheng, W. Y. Y. and Steenburgh, W. J.: Evaluation of Surface Sensible Weather Forecasts by the WRF and the Eta Models over the Western United States, Weather Forecast., 20, 812–821, doi:10.1175/WAF885.1, 2005.

Chen, Y., Ebert, E. E., Walsh, K. J. E., and Davidson, N. E. : Evaluation of TRMM 3B42 precipitation estimates of tropical cyclone rainfall using PACRAIN data, J. Geophys. Res. Atmos., 118, 2184–2196, doi:10.1002/jgrd.50250, 2013

Dinku, T., Ruiz, F., Connor, S. J., and Ceccato, P.: Validation and Intercomparison of Satellite Rainfall Estimates over Colombia, J. Appl. Meteorol. Climatol., 49, 1004–1014, doi:10.1175/2009JAMC2260.1, 2010.

Dinku, T., Ceccato, P., and Connor, S. J.: Challenges of satellite rainfall estimatin over 626 mountainous and arid parts of east Africa, Int. J. Remote Sens., 30, 5965–5979, 2011.

Edzer Pebesma: CRAN – Package gstat, available at: http://cran.r-project.org/web/packages/gstat/index.html (last access: 17 July 2012), 2011.

HESSD
11, 411–449, 2014

Emck, Paul.: A climatology of South Ecuador, Unpublished PhD Thesis, Universität 631 Erlangen, Germany, 2007.
Habib, E., Henschke, A., and Adler, R. F.: Evaluation of TMPA satellite-based research and real-time rainfall estimates during six tropical-related heavy rainfall events over Louisiana, USA, Atmos. Res., 94, 373–388, doi:10.1016/j.atmosres.2009.06.015, 2009.
Haylock, M. R., Hofstra, N., Klein Tank, A. M. G., Klok, E. J., Jones, P. D., and New, M.: A European daily high-resolution gridded data set of surface temperature and precipitation for 1950–2006, J. Geophys. Res., 113, D20119, doi:10.1029/2008JD010201, 2008.
Huffman, G. J., Adler, R. F., Bolvin, D. T., Gu, G., Nelkin, E. J., Bowman, K. P., Hong, Y., Stocker, E. F., and Wolff, D. B.: The TRMM Multisatellite Precipitation Analysis (TMPA): Quasi-Global, Multiyear, Combined-Sensor Precipitation Estimates at Fine Scales, J. Hydrometeorol., 8, 38–55, doi:10.1175/JHM560.1, 2007.
Human, G. J. and Bolvin D. T.: TRMM and other data precipitation data set documentation (last access: 1 December 2013), 2012.
Human, G. J., Adler, R. F., Bolvin, D. T., and Nelkin, E. J: The TRMM multi-satellite precipitation analysis (TMPA), in: Satellite Rainfall Applications for Surface Hydrology, edited by: Gebremichael, M. and Hossain, F., Springer Science, New York, USA, 2010.
Jankov Jr., I., W. A. G., Segal, M., Shaw, B., and Koch, S. E.: The Impact of Different WRF Model Physical Parameterizations and Their Interactions on Warm Season MCS Rainfall, Weather Forecast., 20, 1048–1060, doi:10.1175/WAF888.1, 2005.
Kistler, R., Kalnay, E., Collins, W., Saha, S., White, G., Woollen, J., Chelliah, M., Ebisuzaki, W., Kanamitsu, M., Kousky, V., Van Den Dool, H., Jenne, R., and Fiorino, M.: The NCEP-NCAR 50-year reanalysis: monthly means CD-ROM and documentation, B. Am. Meteorol. Soc., 82, 247–267, 2001.
Li, J. and Heap, A. D.: A Review of Spatial Interpolation Methods for Environmental Scientists, Geoscience Australia„ 200, 137, available at: http://www.ga.gov.au/image_cache/GA12526.pdf, 2008.
Liebmann, B. and Smith, C. A.: Description of a Complete (Interpolated) Outgoing Longwave Radiation Dataset, B. Am. Meteorol. Soc., 77, 1275–1277, 1996.
Maussion, F., Scherer, D., Finkelnburg, R., Richters, J., Yang, W., and Yao, T.: WRF simulation of a precipitation event over the Tibetan Plateau, China – an assessment using remote sensing and ground observations, Hydrol. Earth Syst. Sci., 15, 1795–1817, doi:10.5194/hess-15-1795-2011, 2011.

HESSD
11, 411–449, 2014

Minder, J. R., Durran, D. R., Roe, G. H., and Anders, A. M.: The climatology of small-scale orographic precipitation over the Olympic Mountains: Patterns and processes, Q. J. Roy. Meteorol. Soc., 134, 817–839, 2008

Muñoz, Á. G. and Recalde, C.: OA_NOSA30 dataset, available at: http://iridl.ldeo.columbia.edu/SOURCES/.U_Zulia/.CMC/.OA_NOSA30/.surface/ (last access: 3 May 2012), 2010.

Muñoz, A., Lopez, P., Velasquez, R., Monterrey, L., Leon, G., Ruiz, F., Recalde, C., Cadena, J., Mejia, R., Paredes, M., Bazo, J., Reyes, C., Carrasco, G., Castellon, Y., Villarroel, C., Quintana, J., and Urdaneta, A.: An Environmental Watch System for the Andean countries: El Observatorio Andino, 91, 20, available at: http://arxiv.org/abs/1006.0926, 2010.

Pessacg, N.: Precipitation sensitivity experiments using WRF, 80 pp., University of Buenos Aires, Argentina, 2008 (in Spanish).

Pineda, L., Ntegeka, V., and Willems, P.: Rainfall variability related to sea surface temperature anomalies in a Pacific–Andean basin into Ecuador and Peru, Adv. Geosci., 33, 53–62, doi:10.5194/adgeo-33-53-2013, 2013.

Rollenbeck, R. and Bendix, J.: Rainfall distribution in the Andes of southern Ecuador derived from blending weather radar data and meteorological field observations, Atmos. Res., 99, 277–289, doi:10.1016/j.atmosres.2010.10.018, 2011.

Romilly, T. G. and Gebremichael, M.: Evaluation of satellite rainfall estimates over Ethiopian river basins, Hydrol. Earth Syst. Sci., 15, 1505–1514, doi:10.5194/hess-15-1505-2011, 2011.

Rossel, F. and Cadier, E.: El Nino and prediction of anomalous monthly rainfalls in Ecuador, Hydrol. Process., 23, 3253–3260, doi:10.1002/hyp.7401, 2009.

Rossel, F., Le Goulven, P., and Cadier, E.: Areal distribution of the influence of ENSO on the annual rainfall in Ecuador, Rev. Sci. l'Eau, 12, 183–200, 1999.

Ruiz, J. J., Saulo, C., and Nogués-Paegle, J.: WRF Model Sensitivity to Choice of Parameterization over South America: Validation against Surface Variables, Mon. Weather Rev., 138, 3342–3355, doi:10.1175/2010MWR3358.1, 2010.

Schaefer, J. T.: The Critical Success Index as an Indicator of Warning Skill, Weather Forecast., 5, 570–575, doi:10.1175/1520-0434(1990)005%253C0570:TCSIAA%253E2.0.CO;2, 1990.

Schafer, R., Avery, S. K., and Gage, K. S.: A comparison of VHF wind profiler observations 685 and the NCEP-NCAR Reanalysis over the tropical Pacific, J. App. Meteor., 42, 873–889, 2003.

HESSD
11, 411–449, 2014

Scheel, M. L. M., Rohrer, M., Huggel, C., Santos Villar, D., Silvestre, E., and Huffman, G. J.: Evaluation of TRMM Multi-satellite Precipitation Analysis (TMPA) performance in the Central Andes region and its dependency on spatial and temporal resolution, Hydrol. Earth Syst. Sci., 15, 2649–2663, doi:10.5194/hess-15-2649-2011, 2011.

Skamarock, W. C., Klemp, J. B., Dudhia, J., Gill, D. O., Barker, D. M., Wang, W., and Powers, J. G.: A Description of the Advanced Research WRF Version 2. NCAR Tech note, 2005.

Su, F., Hong, Y., and Lettenmaier, D. P.: Evaluation of TRMM Multisatellite Precipitation Analysis (TMPA) and Its Utility in Hydrologic Prediction in the La Plata Basin, J. Hydrometeorol., 9, 622–640, doi:10.1175/2007JHM944.1, 2008.

Wang, X. L. and Feng, Y.: Software for detection and adjustment of shifts in daily precipitation data series, available at: http://etccdi.pacificclimate.org/software.shtml, 2012.

Wang, X., Chen, H., and Wu, Y.: New techniques for the detection and adjustment of shifts in daily precipitation data series, J. Appl. Meteorol. Climatol., 49, 2416–2436, doi:10.1175/2010JAMC2376.1, 2010.

Ward, E., Buytaert, W., Peaver, L., and Wheater, H.: Evaluation of precipitation products over complex mountainous terrain: A water resources perspective, Adv. Water Resour., 34, 1222–1231, doi:10.1016/j.advwatres.2011.05.007, 2011.

Willems, P.: Quantification and relative comparison of different types of uncertainties in sewer water quality modelling, Water Res., 42, 3539–3551, 2008.

Willems, P.: Model uncertainty analysis by variance decomposition, Phys. Chem. Earth, 42–44, 21–30, 2012.

Willems, P. and Berlamont, J.: Accounting for the spatial rainfall variability in urban modelling applications, Water Sci. Technol., 45, 105–112, 2002.

Wilson, E. M.: Engineering Hydrology, 3rd Ed., Macmillan, 1983.

Yamamoto, J. K.: An alternative measure of the reliability of ordinary kriging estimates, Math. Geol., 32, 489–509, doi:10.1023/A:1007577916868, 2000.

Zulkafli, Z., Buytaert, W., Onof, C., Manz, B., Tarnavsky, E., Lavado, W., and Guyot, J.: A comparative performance analysis of TRMM 3B42 (TMPA) versions 6 and 7 for hydrological applications over Andean-Amazon river basins, J. Hydrometeorol., doi:10.1175/JHM-D-13-094.1, in press, 2013.

HESSD
11, 411–449, 2014

Table 1. Description of sub-catchments and rain gauge density of homogeneous stations.

Code	Sub-catchments	Catchment	Altitudinal range (m)	Area (km^2)	Stations density*
1	Chone	Chone	0–350	3259	0.80
2	Portoviejo	Portoviejo	0–600	3548	1.00
3	Lower Guayas	Guayas	0–680	14 641	0.30
4	Middle Guayas		0–4100	21 423	0.70
5	Upper Guayas		300–4000	3642	2.50
6	Taura	Taura	0–2600	2449	0.40
7	Cañar	Cañar	0–4300	2412	1.50
8	Naranjal-Pagua	Naranjal-Pagua	0–4000	3387	0.01
9	Jubones	Jubones	0–4000	4361	1.20
10	Santa Rosa	Santa Rosa	0–2200	1062	0.80
11	Arenillas	Arenillas	0–1400	653	1.40
12	Zarumilla	Zarumilla	0–800	810	1.10
13	Puyango	Puyango – Tumbes	300–3500	3662	0.50
14	Catamayo	Catamayo – Chira	300–3500	4173	1.70
15	Alamor		200–2300	1182	2.30
16	Macará		150–3600	3166	2.00
17	Quiroz		150–3500	3137	3.70
18	Chira		0–800	4931	0.70
19	Chipillico		100–3200	1179	2.30
20	Tumbes	Puyango – Tumbes	0–1200	8200	0.30
21	Piura	Piura	0–2500	9472	0.30
		Total		100 745	

* Stations per precipitation products grid cell (~ 900 km^2).

HESSD
11, 411–449, 2014

Table 2. Cross-validation results of daily rainfall interpolation for all stations over the period 1998–2008 using inverse distance weighting (IDW), linear regression with altitude (LR), original kriging (OK), and kriging with external drift (KED) techniques.

Method	Correlation	MSE	Performance
IDW	0.260	65.33	0.012
LR	0.275	0.656	0.881
OK	0.210	0.550	0.865
KED	0.484	0.510	0.885

HESSD
11, 411–449, 2014

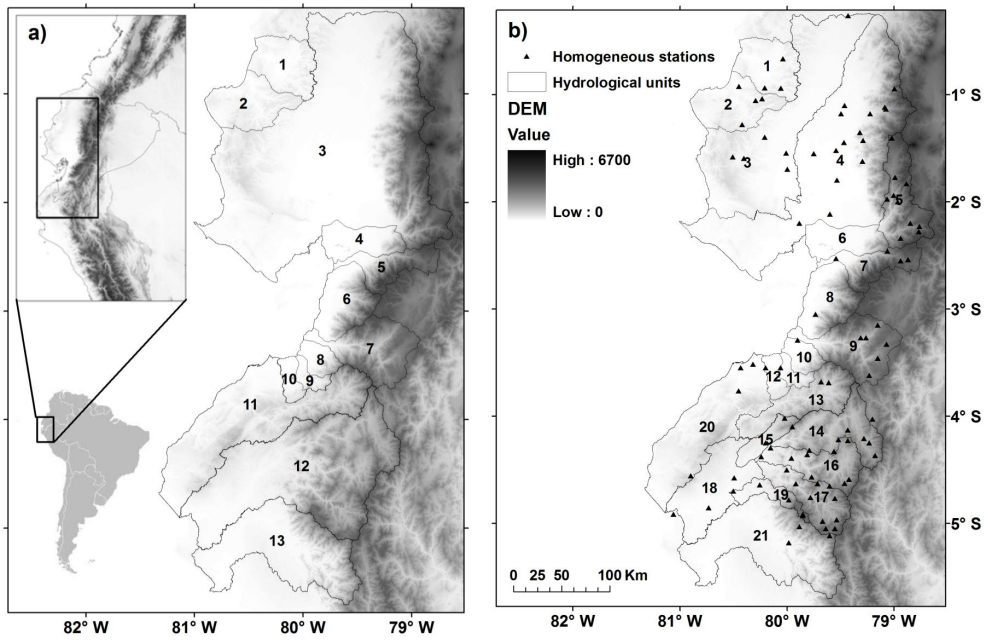

Fig. 1. (a) Location of the study area and the delineation of the Ecuadorian and the Peruvian catchments; **(b)** Distribution of the homogeneous rain gauge stations per sub-catchments of which the codes are detailed in. The Digital Elevation Model (DEM) is derived from the Shuttle Radar Topography Mission (SRTM) with a 92 × 92 m resolution.

HESSD
11, 411–449, 2014

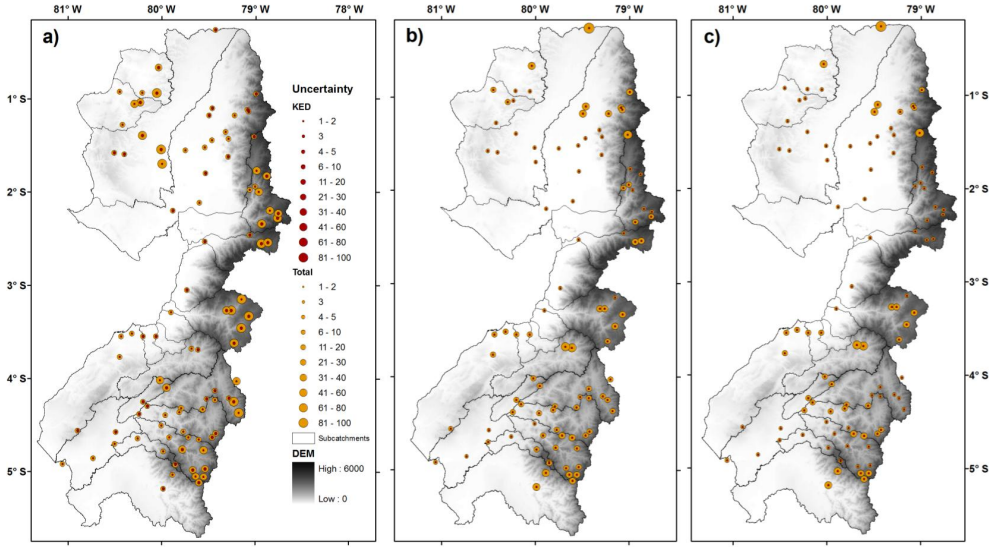

Fig. 2. Spatial distribution of the total residual variance (graded orange circles) and the fractional contribution of the KED uncertainty in the total residual variance (graded red circles) based on the comparison of one-single day random KED simulation against **(a)** OANOSA-30, **(b)** TMPA V6 and **(c)** TMPA V7. Topographic map is gray shaded. The size of the circles is proportional to the variance value.

HESSD
11, 411–449, 2014

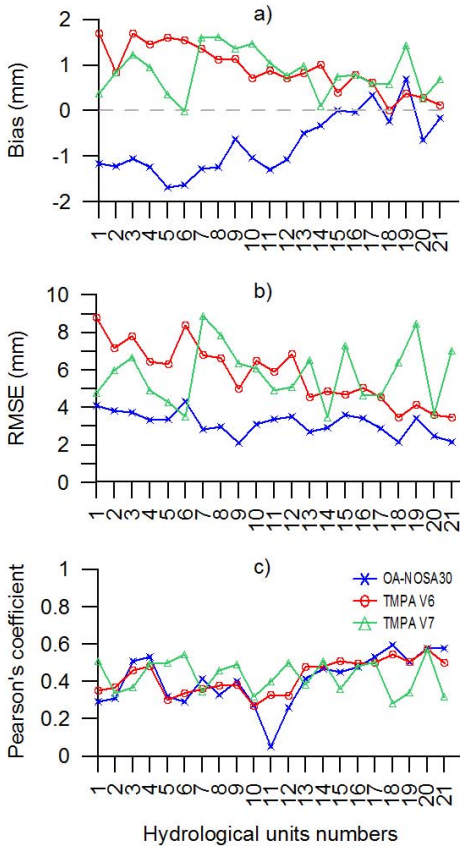

Fig. 3. Overall performance of the daily analysis for TRMM V7, V6 and OA-NOSA30 and precipitation estimates per sub-catchment, averaged over the period 1998–2008. Names of sub-catchments correspnding to the numbers are detailed in Table 1. **(a)** Bias **(b)** RMSE and **(c)** Pearson's correlation coefficient.

HESSD
11, 411–449, 2014

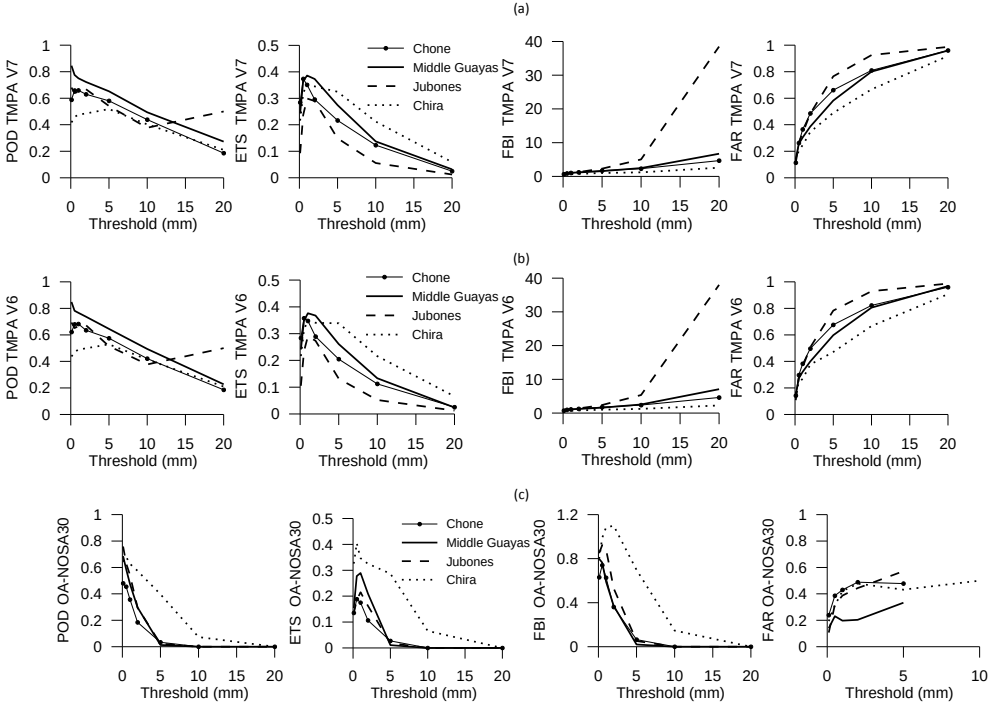

Fig. 4. Precipitation detection indexes (POD, ETS, FBI, and FAR) of daily average for **(a)** TMPA V7, **(b)** V6 and **(c)** OA-NOSA30 outputs against KED interpolated station data averaged over the period 1998–2008, applying different thresholds as precipitation upper limit.

HESSD
11, 411–449, 2014

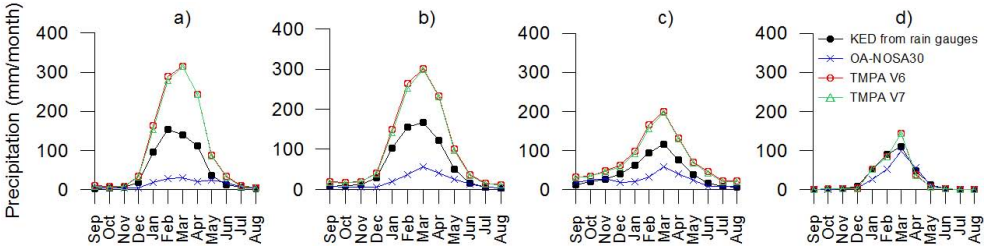

Fig. 5. Mean monthly precipitation in sub-catchments from North to South: **(a)** Chone, **(b)** Middle Guayas, **(c)** Jubones, and **(d)** Chira over the period 1998–2008.

HESSD
11, 411–449, 2014

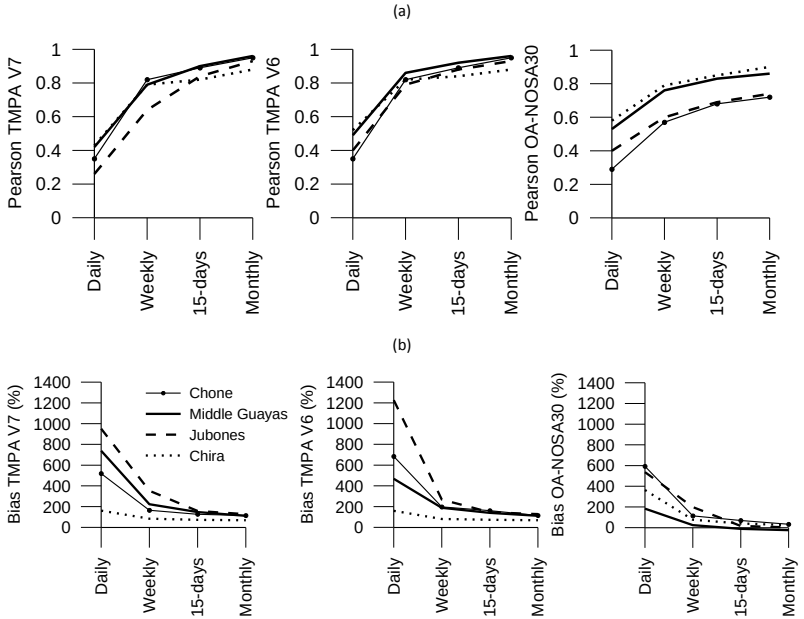

Fig. 6. Overall performance analysis considered for daily, weekly, 15-daily and monthly time aggregations. **(a)** Pearson's correlation coefficient. **(b)** Bias (%) for TMPA V7, V6 and OANOSA-30 products calculated for a representative sub-catchment of the north, centre and south region, mean values over the period 1998–2008.

HESSD
11, 411–449, 2014

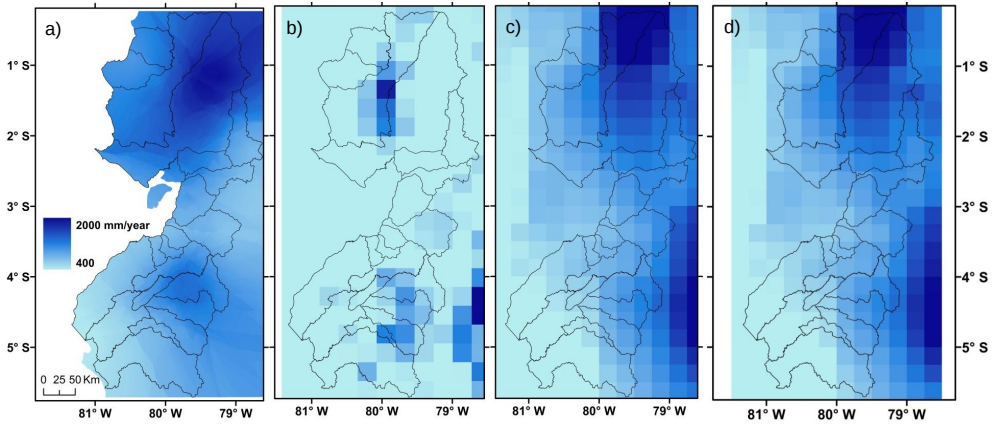

Fig. 7. Spatial distribution of the mean annual precipitation over the period 1998–2008 according to the KED interpolation of 98 rain gauges **(a)**, OA-NOSA30 **(b)**, TMPA V6 **(c)** and TMPA V7 **(d)**.

HESSD
11, 411–449, 2014

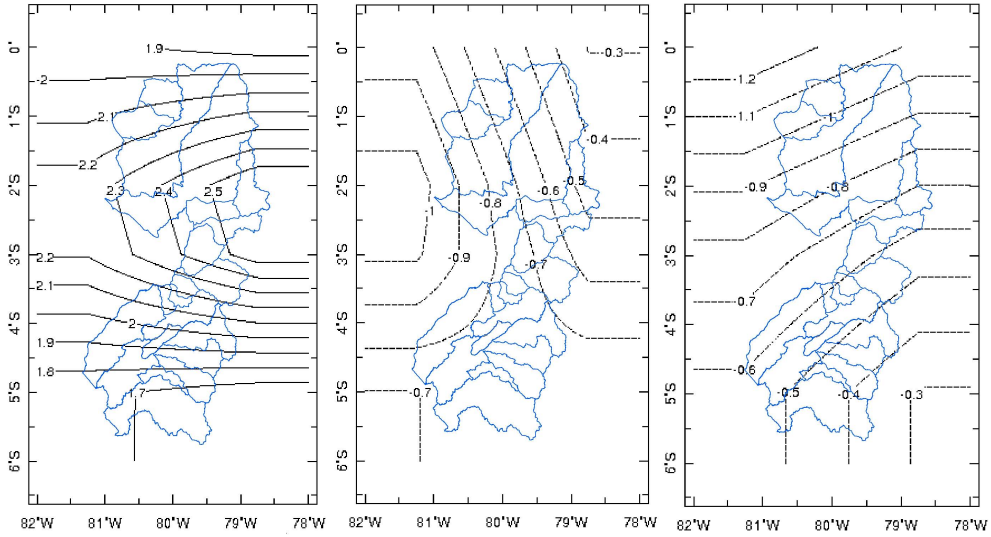

Fig. 8. Monthly anomalies of OLR (Watts m^{-2}) during 1998–2008 within the rainy season December-January(left). February-March (centre). April-May (right).

HESSD
11, 411–449, 2014